Article

Influence of the wave spectrum on statistical wave properties

Tatjana Kokina [1], **Frederic Dias** [1,*]

[1] University College Dublin, School of Mathematics and Statistics, Earth Institute, Belfield, Dublin 4, Ireland

Abstract: The main goal of the paper is to compare the effects of the wave spectrum, computed using the Discrete Interaction Approximation (DIA) and the Webb–Resio–Tracy (WRT) methods, on statistical wave properties such as skewness and kurtosis. The statistical properties are obtained by integrating the three-dimensional free-surface Euler equations with a high-order spectral method combined with a phenomenological filter to account for the energy dissipation due to breaking waves. In addition, we investigate the minimum spatial domain size required to obtain meaningful statistical wave properties. The numerical simulations are performed over a physical domain of size 4.13 km × 4.13 km. The results indicate that statistical properties must be computed over an area of at least 4 km^2. The results also suggest that selecting a more computationally expensive WRT method does not affect the statistical values to a great extent. The most noticeable effect is due to the energy dissipation filter that is applied. It is concluded that selecting the WRT or the DIA algorithm for computing the wave spectrum needed for the numerical simulations does not lead to major differences in the statistical wave properties. However, more accurate energy dissipation mechanisms due to wave breaking are needed.

Keywords: Draupner storm; spectral methods; DIA; WRT; WAVEWATCH III; wave statistics; breaking waves; rogue waves.

1. Introduction

The occurrence and prediction of rogue or freak waves have been investigated extensively in the recent years [1–5]. Rogue or freak waves can be defined as phenomenal waves, either with their height more than twice the significant wave height (SWH) or with their crest height more than 1.25 the SWH. The SWH is the mean of the largest third of the waves in a wave record. Rogue waves are rare events, but should not be underestimated, as they can be very dangerous, due to their spontaneous development and the force with which they can impact on marine vessels and structures. Apart from myths or seaman stories, there was no scientific evidence of rogue waves occurrence until 1995. On 1 January 1995, at 15.00, instruments fitted on the Draupner E platform recorded a 25.6 m rogue wave. The present study concentrates on the Draupner wave to test the influence of physical and numerical parameters used to obtain the statistical wave properties of large waves.

The first important quantity is the wave spectrum that describes the sea state associated with the occurrence of extreme waves. The concept of sea state is defined as either the temporal domain where the wave field is statistically stationary, or the area of the ocean where the wave field is statistically homogeneous. Various methods with different levels of numerical complexity can be used to obtain such spectra. In particular, different methods exist for the computation of the nonlinear quadruplet interactions in the wave spectrum. One of the methods, the Webb-Resio-Tracy (WRT) method [6–8], produces a more accurate physical shape of the power spectrum [9]. It is a more detailed algorithm, compared to the discrete interaction approximation (DIA) method [10], as the WRT algorithm computes the full nonlinear interactions. However, being more detailed, the WRT method is also more computationally expensive.

The wave spectrum is then used to generate an initial sea state. The evolution of the state can be followed by integrating numerically the free-surface Euler equations. Several papers using a

high-order spectral (HOS) method have been published recently, including [11–15]. The physical processes responsible for the formation of rogue waves are still under debate. They include nonlinear focusing [16] and dispersive focusing [17,18]. Recent work has provided evidence that real-world rogue waves, at least those under investigation, can be explained without the modulational instability [13]. Despite the debate about the process responsible for the generation of rogue waves, there is agreement on how the probability of these events can be estimated. Using wave statistics it is possible to estimate the probability of rogue wave occurrence. This is an area of active research, and one can find various publications dedicated to this question [14,19–22]. The present study concentrates on two of the most important statistical parameters, namely the skewness and the kurtosis (see subsection 2.1 for more details). In general, high values of (excess) kurtosis indicate a greater probability of rogue wave occurrence [13,21,22]. A recent study on the skewness can be found in [23].

In this work, we solve the free-surface Euler equations (water wave equations) using a HOS method, see Methods section 4.1 for more details. The initial condition is reconstructed from a hindcast of the Draupner wave, created using the third generation wave model WAVEWATCH III (WW3) with two different energy transfer computation and parametrization methods (section 4.2). The first question we ask is the following: does the shape of the spectrum, different due to differences in the production algorithms, significantly affect the statistical values such as skewness and kurtosis? This is an important question, linked to the justification to use WRT to accurately predict statistical wave properties and rogue wave occurrence. Another question of interest is the minimal size of the spatial domain that is required to obtain meaningful values of the statistical properties.

This paper is organized as follows. First, we present the difference between the two wave spectra used as initial conditions for the HOS model. Then we present the results from the ensemble simulations and the statistical wave properties of interest. Next we discuss the results and their implications on the probability of occurrence of rogue waves. We also discuss the various choices for the energy transfer computation, for the dissipation due to wave breaking and for the spatial domain size. In the Methods section we present the numerical model used for the simulations and the two different wave spectra used in the study. We also provide a brief description of the statistical wave properties.

2. Results

The main objective of this study is to identify differences, if any, in the ocean wave statistics, depending on the initial wave spectra and the different filters for the phenomenological dissipation of wave energy. The initial conditions used for the HOS simulations were obtained from WW3 hindcasts (see the Methods section for more details).

Depending on the method used for the production of the hindcast of the Draupner storm, the shape of the wave spectrum differs. The two hindcasts used to produce initial conditions for the HOS simulations were produced using the DIA [10] and the WRT model [6–8]. More details can be found in the work of Ponce de León & Osborne [9], who clearly observe two high frequency channels (bimodality) in their spectrum. What is not clear is whether bimodality is only due to the wave-wave interaction term S_{nl} or it can also be enhanced by the energy input from wind term S_{in}. The analysis of [9] does not clearly show the weight of the three terms S_{nl}, S_{in} and S_{diss} (energy dissipation due to wave breaking). Figure 1 shows the Draupner wave spectrum produced using WW3 with the DIA method. Figure 2 shows the same spectrum at the same time, but computed using WW3 with the WRT method. Ponce de León & Osborne produce the WW3 spectrum at 14 different 'stations' in the North Sea. In the figures below and throughout the paper we concentrate on the WW3 spectrum for station 1, located at $58.17°(58°10'12'')$ North and $2.47°(2°28'12'')$ East for WW3/DIA-40 and WW3/WRT. The third wave spectrum WW3/DIA-30 used in the simulations was produced at location $58.18°(58°10'48'')$ North and $2.47°(2°28'12'')$ East. The actual Draupner E platform, where the instrument that recorded the famous phenomenal wave height is installed, is located at $58.19°(58°11'19.30'')$ North and $2.47°(2°28'0.00'')$ East. In Figure 3 we plot the difference between the two spectra obtained with two methods mentioned

above. The shape of the difference is explained by the fact that peak frequencies and peak directions for the WW3/WRT-40 and WW3/DIA-40 spectra are slightly different. This causes a shift in the direction axis and results in a dip in the plot along $\theta - \theta_p = 60°$. The three-dimensional wave spectrum produced with WRT has a noticeably higher and sharper peak, and the two high frequency channels are more visible. The higher peak of the WRT spectrum can be explained by the fact that while the WRT method computes the full nonlinear quadruplet interactions the DIA method operates with certain approximations. But we will show below that the statistical values obtained with the DIA and WRT methods do not differ significantly enough to claim that bimodality affects rogue waves.
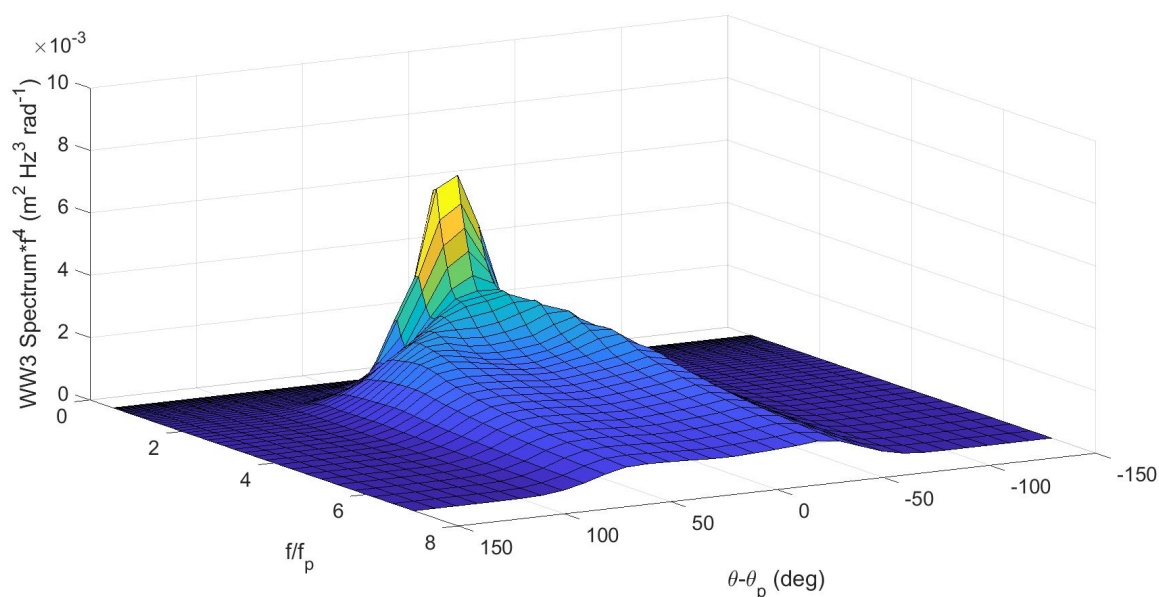
Figure 1. Three-dimensional wave spectrum from the WW3/DIA-40 hindcast for the Draupner storm on 1 Jan 1995 at 15.00, at station 1, $58.17°(58°10'12'')$N $2.47°(2°28'12'')$E. The spectrum has been transformed to a compensated form via multiplication by f^4, where f is the frequency. Frequencies have been made dimensionless by dividing them by the frequency f_p at the peak of the spectrum. The plot is centered around the peak direction θ_p.
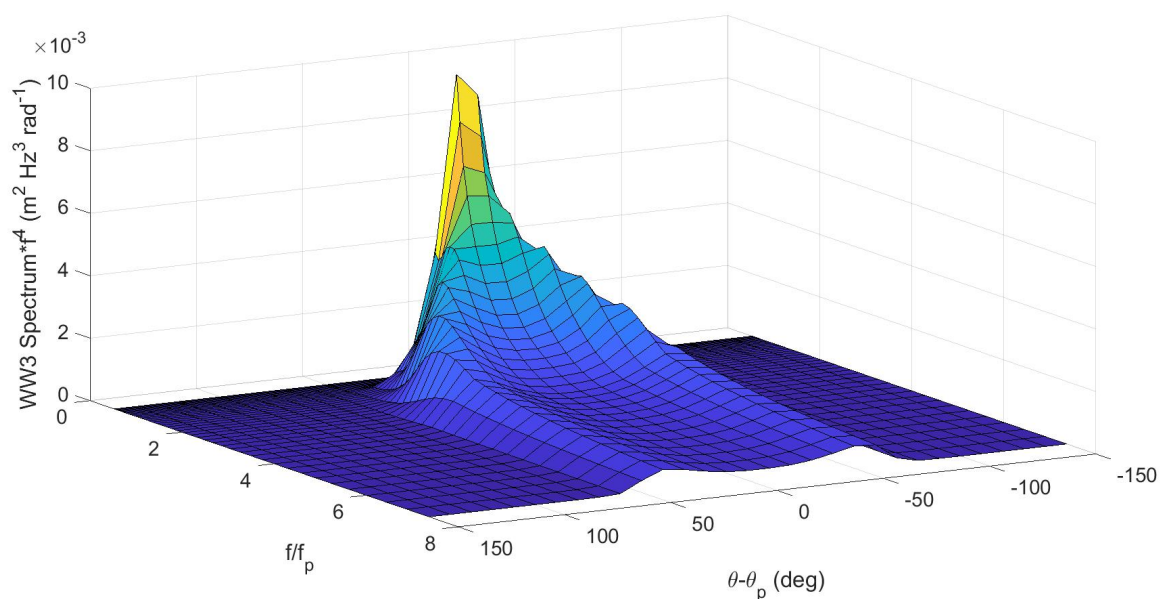
Figure 2. Same as Fig. 1 for the WW3/WRT-40 hindcast for the Draupner storm on 1 Jan 1995 at 15.00. The two high frequency channels are more visible than in the WW3/DIA-40 spectrum.
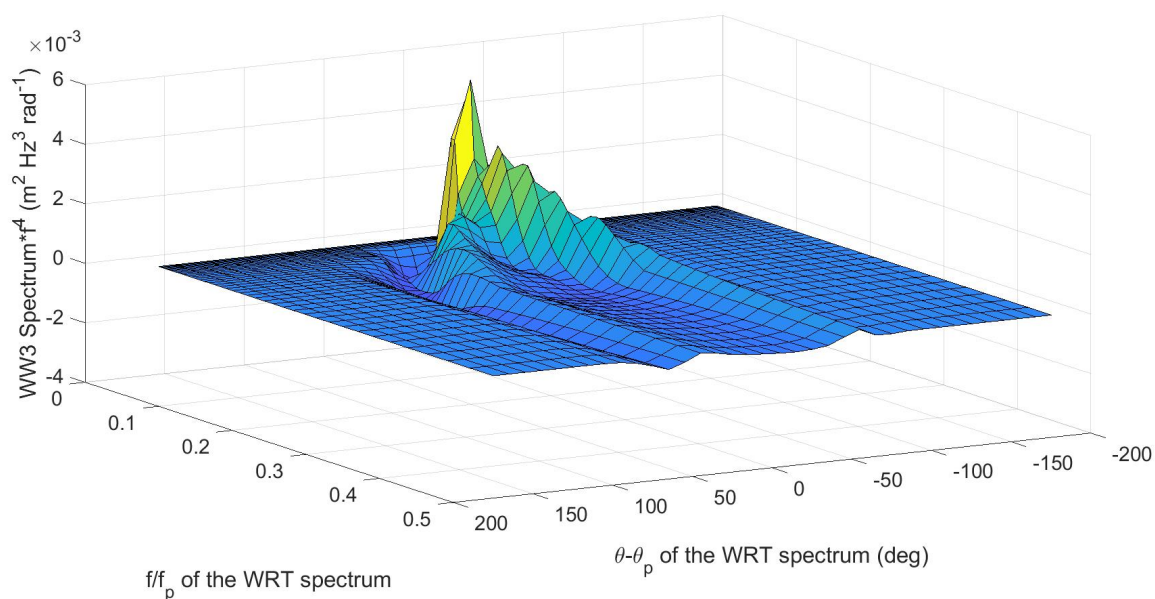
Figure 3. Difference between the WW3/DIA-40 and WW3/WRT-40 spectra shown in Fig. 1 and Fig.2, respectively, for the Draupner storm.

The plot for the WW3/DIA-30 wave spectrum is not included here as the shape of the DIA-30 spectrum is very similar to that of the DIA-40 spectrum. The two wave spectra plotted above, as well as the DIA-30 spectrum and a different wave spectrum for another event in Ireland on 1 March 2017 (DIA-32), were all used in the HOS simulations. The event of 1 March 2017 belongs to the storm that Met Éireann named Storm Ewan. Note that Ewan wasn't a particularly strong storm.

2.1. Statistical moments

In this subsection, we present the results of the calculated skewness and kurtosis for both strong and weak filters used for the phenomenological dissipation of wave energy. The results are summarised

in Table 1. The statistical values are estimated from an ensemble of 20 HOS simulations each. The calculations take into account the time needed for the development of the nonlinearities, as described in the Methods section.

Table 1. Kurtosis and skewness average values for an ensemble of 20 HOS simulations for each set up.

Wave Spectrum	Filter	Kurtosis	Skewness
DIA-30	Strong	3.035	0.144
DIA-40	Strong	3.040	0.149
WRT-40	Strong	3.038	0.156
DIA-30	Weak	3.078	0.165
DIA-40	Weak	3.088	0.173
WRT-40	Weak	3.096	0.182
DIA 1 March 2017	Strong	3.002	0.092
DIA 1 March 2017	Weak	3.051	0.130

2.1.1. Kurtosis for the Draupner sea state

As mentioned earlier, the present study pays particular attention to the fourth statistical moment, namely kurtosis. A rogue wave regime is a more likely to occur only if the surface spectrum is sufficiently narrow-banded and it is characterized by a relatively large positive excess kurtosis [21]. Here, as we are interested in forecasting the sea state, it is of particular interest to compare which wave spectrum (DIA or WRT) is more accurate in its predictions. This has practical implications, as numerical simulations using the WRT method are much more computationally expensive.

In Figs 4 and 5 we show the time evolution of kurtosis calculated from the HOS simulations with strong and weak filters respectively. The simulations were performed for 30 minutes of real time (roughly 120 peak wave periods). Time is normalized by the peak wave period T_p of the spectrum. The vertical axis represents the average value of kurtosis over an ensemble of 20 HOS simulations. The strong and weak filters are described in the Methods section.
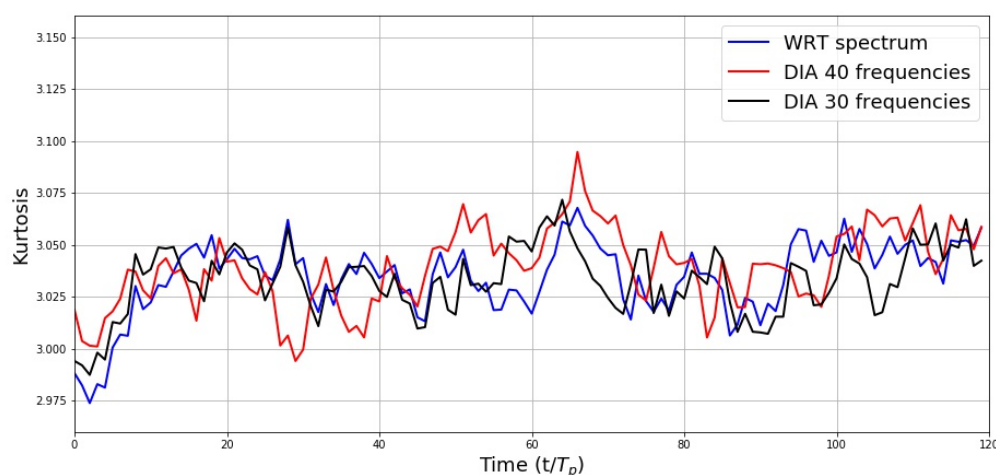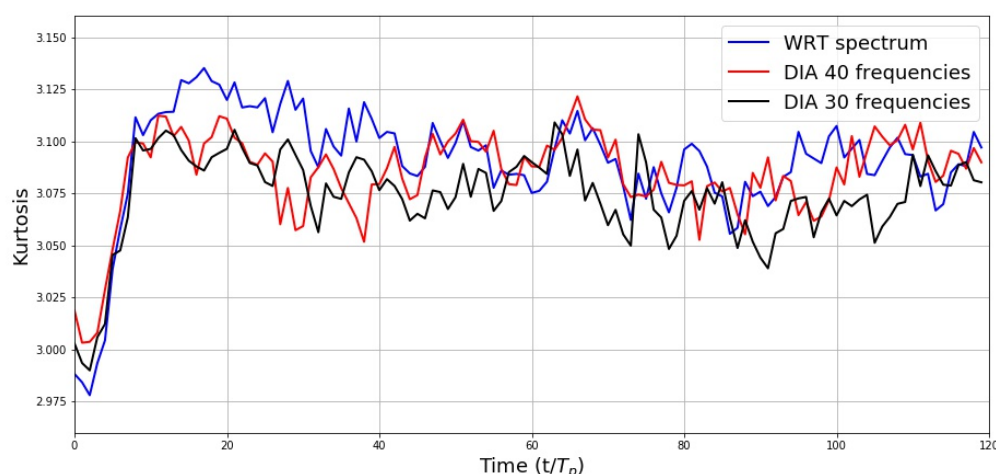

Figure 4. Time evolution of kurtosis for the Draupner sea state, for three different wave spectra and the use of the strong energy filter. Time is normalized by the peak wave period T_p of the spectrum. The statistical parameters are estimated from an ensemble of 20 HOS simulations. The initial artificial transients are excluded from the ensemble averages as they are the result of a ramping function applied to the HOS equations to smoothly activate nonlinearities.

Looking at the strong filter simulations (Fig. 4), we can see that the overall behaviour of kurtosis is similar for the three different input spectra. The numerical values do not deviate from each other. The initial slight growth of the average kurtosis can be seen for all three spectra in the first ≈ 140 seconds. Then the average kurtosis is essentially constant, apart from expected small fluctuations.

The three average values of kurtosis over the whole duration of the simulations that are given in Table 1 are in good agreement. Note that the initial artificial transients are excluded from the averaging process as they are the result of a ramping function applied to the HOS equations to smoothly activate nonlinearities.

In Fig. 5, we compare the time evolutions of kurtosis with the application of the weak filter. With the weak filter we see a much sharper increase in the average kurtosis value in the first ≈ 140 seconds from values around 3 to 3.1. The computations performed with the WRT spectrum display higher values for kurtosis for the most of the simulation time. The computations performed with the DIA-30 spectrum seem to display slightly lower values of kurtosis. The three average values of kurtosis given in Table 1 show that the weak filter leads to a larger difference between the average values. In future work, it will be interesting to extend the simulations beyond the 30 minutes of real time to study the long-term behaviour of the statistical values. In addition, of course, it would be beneficial to increase the size of the ensembles. Note however that if the simulations are run over a longer time, it is legitimate to include wind forcing. Unfortunately, the authors are not aware of any HOS code that can incorporate successfully wind forcing.

Figure 5. Same as Fig. 4 with the use of the weak energy filter.

### 2.1.2. Skewness for the Draupner sea state

Next, we turn our attention to the skewness and perform the same comparisons for the DIA-30, DIA-40 and WRT wave spectra. The time evolution of skewness calculated from the HOS simulations with strong and weak filters, respectively, is presented in Figs 6 and 7, respectively.
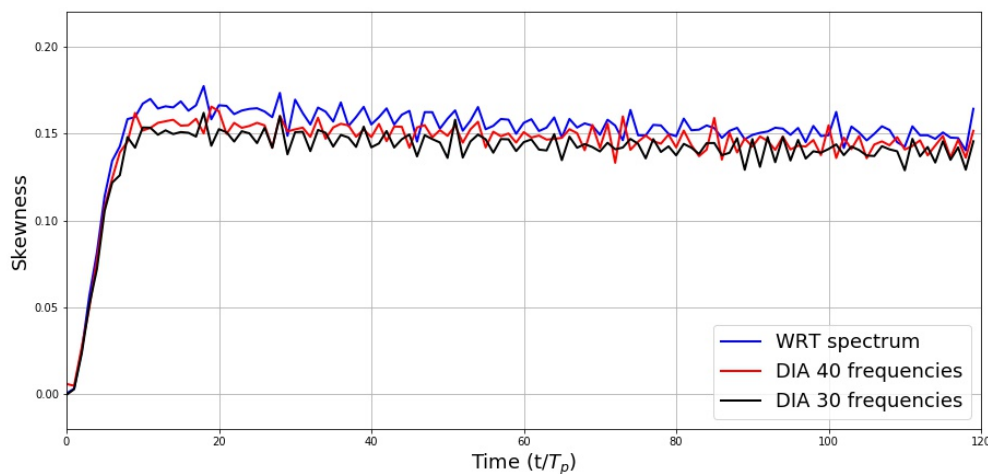
Figure 6. Time evolution of skewness for the Draupner sea state, for three different wave spectra and the use of the strong energy filter. Time is normalized by the peak wave period T_p of the spectrum. The statistical parameters are estimated from an ensemble of 20 HOS simulations. The initial artificial transients are excluded from the ensemble averages as they are the result of a ramping function applied to the HOS equations to smoothly activate nonlinearities.

In Fig. 6, we present the time evolution of the skewness averaged over the ensemble of 20 HOS simulations for the three different input spectra. Time is normalized by the peak period T_p of the spectrum. The first noticeable feature is the sharp increase in the first ≈ 140 seconds of the simulation. This is again due to the ramping function [24] discussed in the Methods section. This transient period corresponding to the development of nonlinearities is excluded from the average value calculations presented in Table 1. All three spectra display a similar time evolution. The skewness decreases slowly as time evolves. The trend is the same for all three cases. The values obtained from the simulations with the WRT-40 spectrum are slightly above the other two for the duration of the simulation, with an average value of 0.156.

In Fig. 7 we repeat the comparisons with the weak filter. The behaviour is similar to the one with the strong filter. However, we note higher values of skewness. This is expected, since less energy is dissipated when the weak filter is applied [25]. Again, we see that the values obtained with the WRT-40 spectrum are slightly above the others most of the time, and the difference in the total average values is slightly higher compared to that with the strong filter. The average value for skewness for the simulations using the DIA-30 spectrum is 0.165. This is an interesting result: using the approximation introduced by Tayfun in [26], the estimated skewness for the Draupner event is 0.165, which is exactly the same value. Hence, the simulations with the DIA-30 spectrum and the weak filter are in perfect agreement with [26].
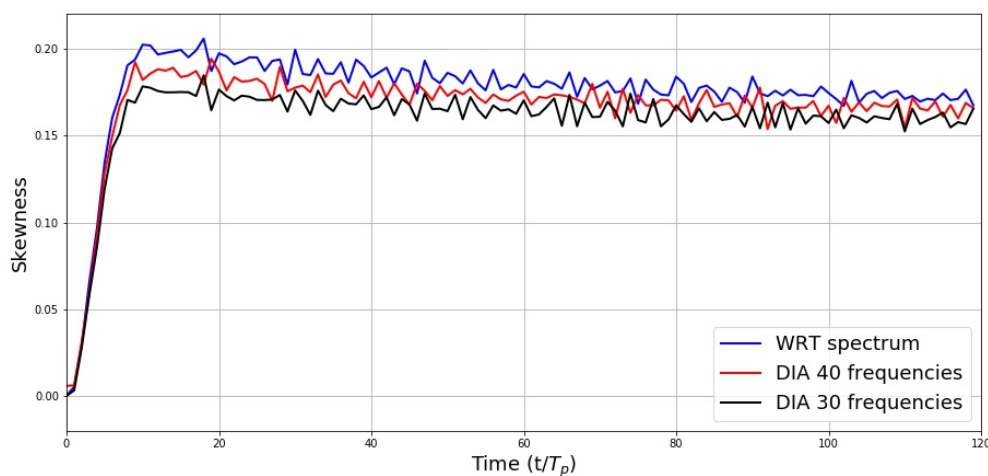
**Figure 7.** Same as Fig. 6 with the use of the weak energy filter.

2.1.3. Statistical parameters of the sea state on 1 March 2017 in Ireland

We also ran the same suite of simulations with a different input spectrum (DIA-32) for a sea state off the west coast of Ireland on 1 March 2017. The coordinates of the location are 54.2856^o North, -10.27^o East. The location is inside the Atlantic Marine Energy Test Site (AMETS) which is being developed by Sustainable Energy Authority of Ireland (SEAI) to facilitate testing of full scale wave energy converters in an open ocean environment. The input spectrum was produced using WW3 again, with a DIA scheme. Details of the wave spectrum can be found in the Methods section.
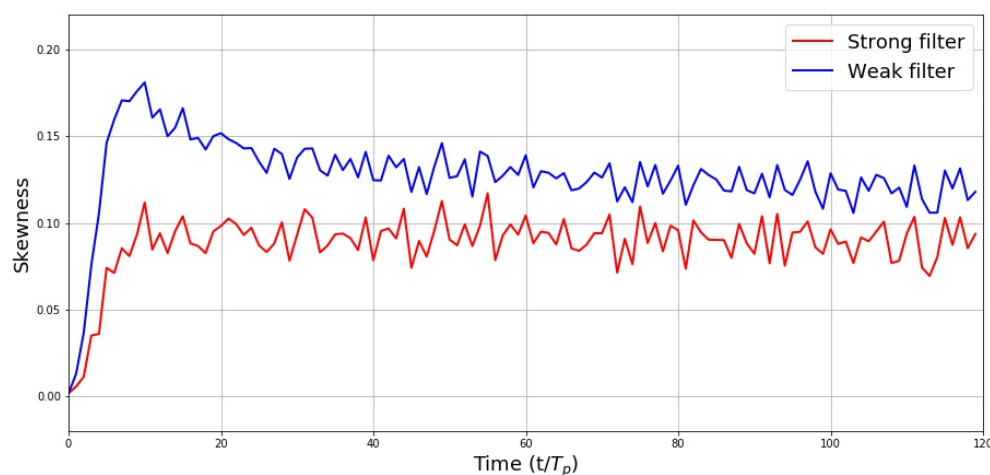
The time evolution of kurtosis is shown with the use of both the strong and weak filters in Fig. 8. The ensemble averages are presented in Table 1 under DIA 1 March 2017. The general behaviour shown in Fig. 8 follows the same pattern as in the Draupner sea state: With the use of the weak filter, the kurtosis increases more quickly and the average values for the kurtosis are higher.

The time evolution of skewness is shown in Fig. 9. Again, a sharper and higher increase is present in the first ≈ 140 seconds of the simulations performed with the weak filter. The values stabilise after 350 seconds and, as expected, values obtained with the weak filter are higher throughout the whole duration of the simulations.
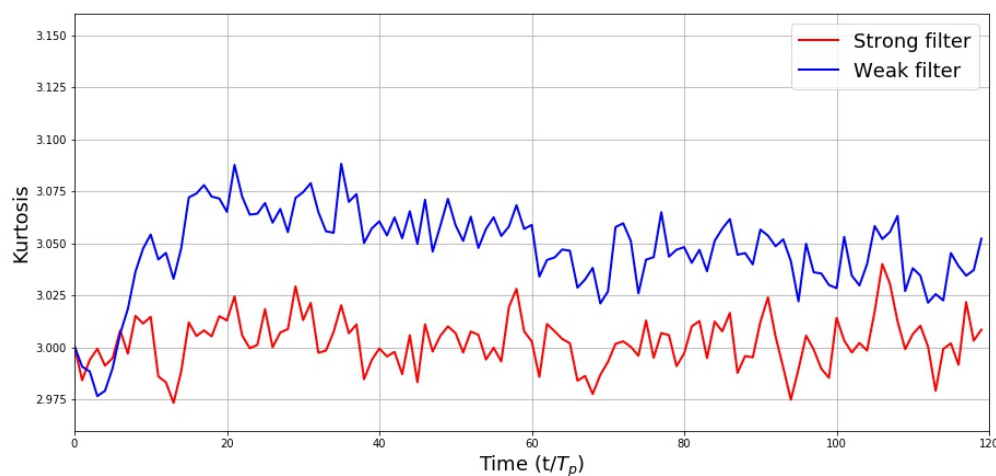
Figure 8. Time evolution of kurtosis for the sea state of 1 March 2017, Ireland, with the use of both the strong and weak energy filters. Time is normalized by the peak wave period T_p of the spectrum. The statistical parameters are estimated from an ensemble of 20 HOS simulations.

Figure 9. Same as Fig. 8 for the time evolution of skewness.

2.2. Spatial domain size

One of the questions we address in the present study is that of the minimal spatial domain size which is acceptable for a meaningful estimation of kurtosis. Using the DIA-30 strong filter simulations of the Draupner sea state, we calculated the kurtosis starting with a 100 m × 100 m square and then increasing the size of the domain in steps of 100 m. The values of kurtosis as a function of the size of the domain are shown in Fig. 10. The horizontal axis represents the size of the side of the square on which the kurtosis value is calculated. In other words, 100 m, for example, refers to a 0.01 km^2 square. The maximum domain size used in the simulations was 4,130 m × 4,130 m, or just slightly over 17 km^2.
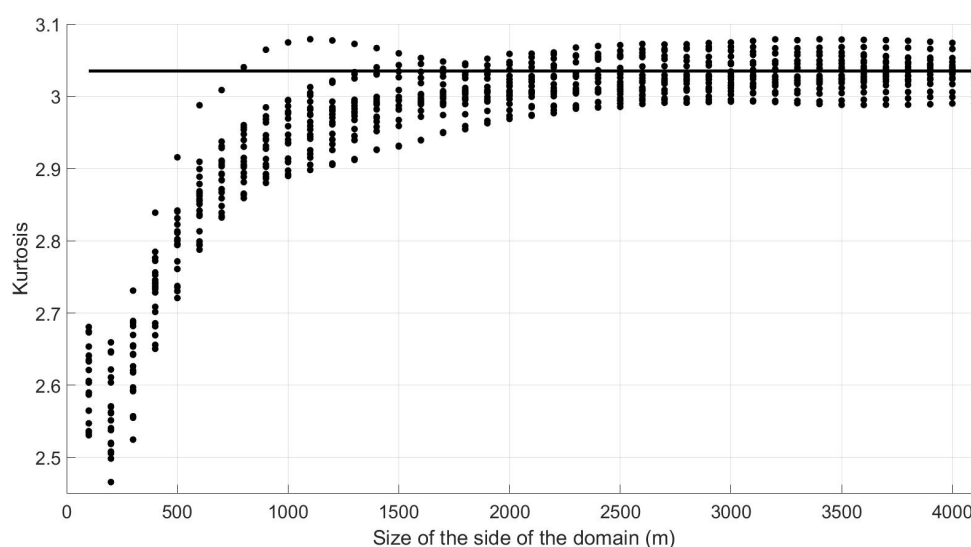
Figure 10. Kurtosis as a function of the size of the spatial domain. The horizontal solid line represents the average value of kurtosis from all 20 simulations of the ensemble using the DIA-30 spectrum and the strong filter. Different circles along a given vertical line represent the 20 simulations at each step size.

For a square of 1000 m × 1000 m, none of the simulations reach the value of 3 for the kurtosis except for one outlier. However, as the domain size increases, all simulations seem to converge, and starting at about 3000 m, the spread is almost uniform. The average simulation values tighten around the average value of all simulations. A zoom-in is given in Fig. 11 for square sides ranging from 1000 m to 4130 m. In Fig. 12, we plot the same results as in Figure 11 with the $x-$axis being a semi-log 1/size of the domain. It looks like the value for mean kurtosis varies linearly as a function of the log of 1/size.

The conclusion is that meaningful values of mean kurtosis are acceptable for squares larger than 2000 m × 2000 m. In other words, the same way that it requires long time series to obtain good estimates of mean kurtosis, it requires large enough domain sizes to obtain good estimates of mean kurtosis.
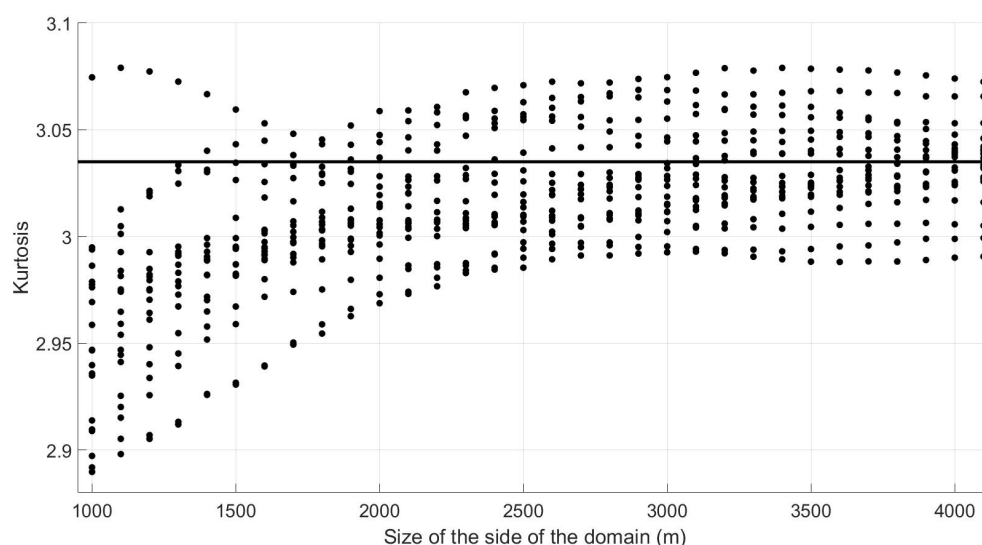
Figure 11. Same as Fig. 10 with a zoom-in on square sides ranging from 1000 m to 4000 m.
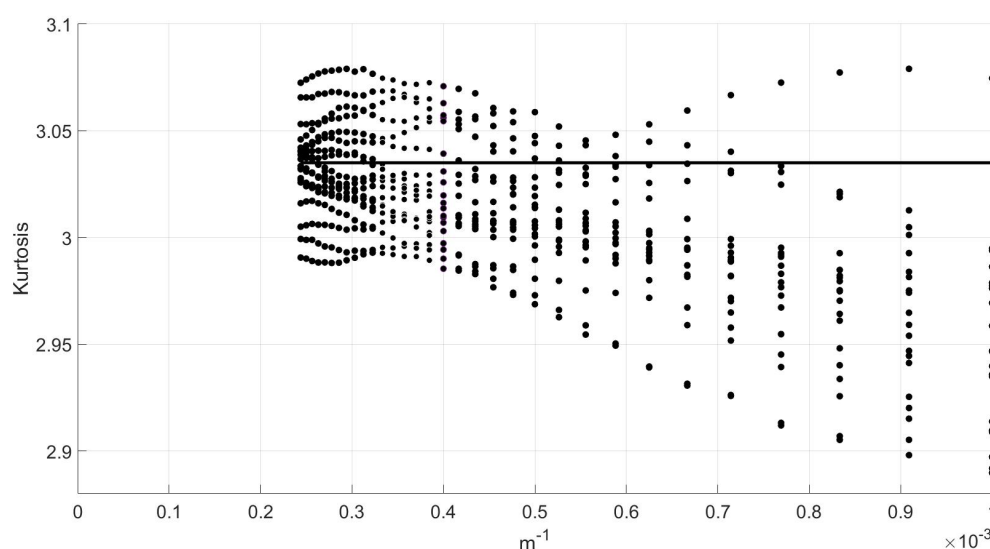
Figure 12. Same as Fig. 11 with a semi-log plot.

3. Discussion

We have presented statistical wave properties for an energetic event, the Draupner storm, using different input parameters. We looked at the behaviour of said properties depending of the wave spectrum, energy dissipation filter, and physical domain size. The question we have in mind is: In a broad sense, what parameters should one use to be able to forecast extreme events accurately, yet with reasonable computational costs?

Two parametrization methods for nonlinear wave energy transfer were considered, and in our results there was no evidence of a critical difference between the two. This can serve as a contribution to reduction in computational costs, since, as mentioned earlier, WRT is much more expensive, but the statistical parameters obtained from the simulations do not indicate a vital need to use the WRT over DIA method in such simulations. Further reduction in computational costs can be obtained from selecting the appropriate physical domain, and we have shown that one should consider the size of the domain carefully, to obtain realistic statistical values. In the particular event we considered (the Draupner storm sea state), the mean wavelength is ≈ 200 meters. If we extrapolate, we could say that the spatial domain should be at least 10 times the wavelength to obtain meaningful statistical values. It would be interesting to extend this question to the time domain - how long should the simulations be in real time, to produce a meaningful result. Fedele et al. [21] determined a so-called optimal sea state duration based on the rationale that variation of key statistics is minimal between two consecutive sea-state sequences. If it is too short, it is meaningless. If it is too long, an implicit assumption of stationarity is made, which is not necessarily satisfied.

The most interesting part of the study is the phenomenological energy dissipation due to breaking and the two filters implemented in the model. As discussed, the HOS method is unable to deal with wave breaking, but we know that breaking is happening, and to account for the energy dissipation due to breaking, filters are employed. We see how the statistical wave properties increase, if less energy is dissipated, but both filters are an 'approximation'. They can be good filters, but still do not fully represent breaking waves. Following recent work on wave breaking onset [27] and on wave breaking strength [28], future work will include the inclusion of this breaking onset threshold parameter, to reflect the energy dissipated more accurately. Indeed, it is important to take into account wave breaking as precisely as possible, especially when one tries to forecast rogue waves, since wave breaking reduces wave growth and impedes the occurrence of rogue waves.

We hope our results will motivate further research into the subject, with longer simulations, larger ensembles, more accurate wave breaking energy dissipation mechanisms and the inclusion of wind forcing in HOS codes.

4. Methods

In this section we discuss the numerical method, the initial conditions used for the numerical simulations, and the post processing of the simulated data.

4.1. Higher Order Spectral Method

In this study we utilize the higher order spectral (HOS) method that was developed independently by Dommermuth & Yue [29] and West et al. [30] in 1987. The version of West et al. was used in this study. The detailed description of the method can be found in Tanaka [31].

The HOS method is a pseudo spectral method that solves the incompressible Euler equations. Starting with the 3D water-wave problem, the problem is reduced to 2D, by evaluating the quantities of interest on the sea surface. Denoting the two horizontal coordinates as x and y and the vertical coordinate as z, the governing equations are

$$\nabla^2 \phi = 0 \qquad\qquad -\infty < z < \eta(x,y,t), \tag{1}$$

$$\phi_t + gz + \frac{1}{2}(\nabla \phi)^2 = 0 \qquad\qquad z = \eta(x,y,t), \tag{2}$$

$$\eta_t + \nabla_h \phi . \nabla_h \eta = \phi_z \qquad\qquad z = \eta(x,y,t). \tag{3}$$

The velocity potential $\phi(x,y,z,t)$ describes the irrotational flow of an inviscid and incompressible fluid, and in the domain of the fluid satisfies the Laplace equation. In addition, at the free surface $\eta(x,y,t)$, the velocity potential satisfies the kinematic and dynamic boundary conditions. Hence, the fluid flow dynamics is described by the above equations (1)-(3), where ∇_h stands for the gradient in the $x - y$ plane.

Introducing the velocity potential on the free surface as

$$\psi(x,y,t) = \phi(x,y,z=\eta,t) \tag{4}$$

allows to rewrite the boundary conditions at the free surface as follows:

$$\psi_t + g\eta + \frac{1}{2}W^2 \left[1 + (\nabla_h \eta)^2\right] = 0, \tag{5}$$

$$\eta_t + \nabla_h \psi . \nabla_h \eta - W \left[1 + (\nabla_h \eta)^2\right] = 0, \tag{6}$$

where W is the vertical velocity on the free surface:

$$W = \left.\frac{\partial \phi}{\partial z}\right|_{z=\eta(x,y,t)}. \tag{7}$$

The main part of the computation is spent solving equations (5) and (6). Spatial derivatives are computed in spectral space while everything else is computed in physical space. This requires mapping back and forth from physical to spectral space. This is achieved in an efficient way using fast Fourier transforms and their inverse transforms. The simulations were performed using 1024×1024 Fourier modes. The spatial domain was set at 4130 m $\times$ 4130 m. The simulation time was 1800 s. An ensemble of 20 simulations for each set up was chosen.

During the simulations the nonlinear terms in equations (5) and (6) are smoothly activated by the Dommermuth ramping function [24].

As described above, the HOS method is unable to deal with wave breaking, as discontinuous surfaces are not permitted. In order to account for energy dissipation due to wave breaking, a low pass filter proposed by Xiao et al. [12] is adopted in the simulations, where k_p is the peak wavenumber:

$$F(\mathbf{k}|k_p, f_1, f_2) = \exp\left(-\left|\frac{\mathbf{k}}{f_1 k_p}\right|^{f_2}\right) \tag{8}$$

Varying the parameters f_1 and f_2 results in energy dissipation that is in agreement with several numerical and experimental works [32–34]. In this study, two filter set ups were used, $F1 = [8, 30]$ and $F3 = [30, 10]$, which are referred to as strong and weak filters respectively. The strong filter shows good correlation with experimental work mentioned above, see [25] for more details. However, the weak filter results in a reduced energy loss. We compare the results obtained with applying both strong and weak filters in the Results section.

Initial conditions for the simulations are obtained from the output of WW3, which is described in the following sections.

4.2. Energy/Action Balance Equation

We are interested in finding better indicators, or improving the current ones, for rogue wave appearance. To forecast a certain event, we would need to follow the evolution of the sea state from the initial given position. In the evolution of the sea state, we need to be able to account for the effects of energy transfers. To approach this we want to see how the energy of the wave evolves with time. There are two approaches as how the energy balance of the waves can be formulated - Lagrangian and Eulerian. If we look at the energy evolution equation and differentiate it with respect to time, i.e. look at the evolution of the energy equation, this will be equal to a term representing all the effects on energy generation or dissipation, such as wind, wave-wave interactions, dissipation due to breaking. We can write this equation as

$$\frac{dE(f, \theta; x, y, t)}{dt} = S(f, \theta; x, y, t) \tag{9}$$

where $S(f, \theta; x, y, t)$ is often written as

$$S = S_{in} + S_{nl} + S_{diss} \tag{10}$$

where S_{in} represents the energy input from wind, S_{nl} represents the wave-wave interactions, and S_{diss} is energy dissipation due to wave breaking.

4.3. Details of the wave spectrum used in the simulations

In the simulations we have used four different wave spectra. When we refer to DIA-30, we mean the Draupner storm hindcast produced using the WW3 model, which was developed at NOAA/NCEP [35,36]. This particular wave spectrum was produced utilizing the DIA method [10] for the computation and parametrization of the nonlinear energy transfer. This model has 36 directional bands, and 30 frequencies, with minimum frequency of 0.0350 Hz up to 0.5552 Hz (see [13] for more details).

The DIA-40 wave spectrum is again a Draupner storm hindcast produced using the WW3 operational wave model with the DIA method, and the WRT-40 spectrum represents the same event but with the WRT [6–8] model for the nonlinear energy transfer. More details on the production of the DIA-40 and WRT-40 wave spectra can be found in [9]. Both hindcasts have 36 directional bands (same as DIA-30) and 40 frequencies, with minimum frequency of 0.0350 Hz up to 0.4898 Hz.

The fourth wave spectrum was produced in house, using again the WW3 model. The spectrum was produced using the DIA method. The model has 24 directional bands, and 32 frequencies, with minimum frequency of 0.0373 Hz up to 0.71595 Hz.

Let's now review briefly the formulations of the DIA and WRT algorithms. They refer to different treatments of the S_{nl} term, that is the energy transfer due to nonlinear wave-wave interactions. The need for parametrization of the S_{nl} terms arises from the length of time required to compute the term exactly.

One of the existing parametrizations was introduced by Hasselmann [10] - the discrete interaction approximation. In his approach Hasselmann arrives at the following:

$$\delta S_{nl} = -2 \frac{\triangle f \triangle \phi}{\triangle f \triangle \phi}$$

$$\delta S_{nl}^+ = (1 + \lambda) \frac{\triangle f \triangle \phi}{\triangle f^+ \triangle \phi}$$

$$\delta S_{nl}^- = (1 - \lambda) \frac{\triangle f \triangle \phi}{\triangle f^- \triangle \phi}$$

$$\times C g^{-4} f^{11} \left[F^2 \left(\frac{F_+}{(1+\lambda)^4} + \frac{F_-}{(1-\lambda)^4} \right) - 2 \frac{F F_+ F_-}{(1-\lambda^2)^4} \right]$$

where C is a numerical constant, $\triangle f, f^+, f^-$ denote the discrete resolution of the spectrum and source function at the frequencies f, f^+, and f^-. The net S_{nl} is calculated by summing over all frequencies, directions, and interaction configurations. For a comparison of the approximate and the exact transfer source function, see [10].

The other parametrization of the S_{nl} term was developed by Webb, Resio, and Tracy [6–8]. Following the mentioned work, one can see that it is beneficial to examine fluxes of action (or energy) past a specific frequency in addition to looking at a source function for the entire spectrum. The energy flux is written as an integral of the density function product with a combination of the Heaviside functions dependent on wavenumber permutations. And then the S_{nl} source can be calculated as the one-dimensional divergence of energy flux:

$$S_{nl}(f) = \frac{\partial [\Gamma_E^+(f) + \Gamma_E^-(f)]}{\partial f} . \tag{11}$$

For more details, see [6–8].

4.4. Statistical wave properties

Two quantities of particular interest in this study are the skewness λ_3 and kurtosis (or excess kurtosis) λ_{40}. These are known as the statistical moments, and are defined as

$$\lambda_3 = \frac{< \eta^3 >}{\sigma^3} , \tag{12}$$

$$\lambda_{40} = \frac{< \eta^4 >}{\sigma^4} - 3 . \tag{13}$$

The angle brackets stand for statistical averages, and σ is the standard deviation of the surface wave elevation.

Plots present in the current work represent full kurtosis, rather than excess. Hence, the plots available in the results section show $\lambda_{40} + 3$. As we are dealing with third-order nonlinear random seas, the excess kurtosis λ_{40} is made up of two components:

$$\lambda_{40} = \lambda_{40}^d + \lambda_{40}^b , \tag{14}$$

where λ_{40}^d represents the dynamic component and λ_{40}^b is the bound harmonic contribution. It has been shown previously that λ_{40}^b is a small number [22]. The contribution λ_{40}^b comes from the Stokes bound harmonic contribution [37].

The statistical averages are performed over the entire spatial domain (except when we study the influence of the size of the spatial domain for kurtosis) over 20 simulations for each set up. The values presented in Table 1 take into account the time needed for the nonlinearities to develop. This is due to the use of the Dommermuth ramping function [24] mentioned in the above section.

References

1. O'Brien, L.; *et al.* Extreme wave events in Ireland: 14680 BP–2012. *Nat. Hazards Earth Syst. Sci.* **2013**, *13*, 625–648. doi:10.5194/nhess-13-625-2013.

2. O'Brien, L.; *et al.* Catalogue of extreme wave events in Ireland: revised and updated for 14680 BP to 2017. *Nat. Hazards Earth Syst. Sci.* **2018**, *18*, 729–758. doi:10.5194/nhess-18-729-2018.

3. Cousins, W.; Onorato, M.; Chabchoub, A.; Sapsis, T.P. Predicting ocean rogue waves from point measurements: An experimental study for unidirectional waves. *Phys. Rev. E* **2019**, *99*, 032201. doi:10.1103/PhysRevE.99.032201.

4. Dudley, J.M.; Genty, G.; Mussot, A.; Chabchoub, A.; Dias, F. Rogue waves and analogies in optics and oceanography. *Nature Reviews Physics* **2019**, *1*, 675–689. doi:10.1038/s42254-019-0100-0.

5. Didenkulova, E. Catalogue of rogue waves occurred in the World Ocean from 2011 to 2018 reported by mass media sources. *Ocean & Coastal Management* **2020**, *188*, 105076. doi:https://doi.org/10.1016/j.ocecoaman.2019.105076.

6. Webb, D., J. Non-linear transfers between sea waves. *Deep Sea Research* **1978**, *25*, 279 – 298.

7. Tracy, B.A.; Resio, D.T. Theory and Calculation of the Nonlinear Energy Transfer between Sea Waves in Deep Water. WES Report; , 1982; Vol. Volume 11.

8. Resio, D.; Perrie, W. A numerical study of nonlinear energy fluxes due to wave-wave interactions Part 1. Methodology and basic results. *Journal of Fluid Mechanics* **1991**, *223*, 603–629. doi:10.1017/S002211209100157X.

9. Ponce de Leon, S.; Osborne, A.R. Role of Nonlinear Four-Wave Interactions Source Term on the Spectral Shape. *J. Mar. Sci. Eng.* **2020**, *8*, 251. doi:10.3390/jmse8040251.

10. Hasselmann, S.; Hasselmann, K.; Allender, J.H.; Barnett, T.P. Computations and Parameterizations of the Nonlinear Energy Transfer in a Gravity-Wave Spectrum. Part II: Parameterizations of the Nonlinear Energy Transfer for Application in Wave Models. *Journal of Physical Oceanography* **1985**, *15*, 1378–1391.

11. Toffoli, A.; Bitner-Gregersen, E.; Osborne, A.; Serio, M.; Monbaliu, J.; Onorato, M. Extreme waves in random crossing seas: Laboratory experiments and numerical simulations. *Geophys. Res. Lett.* **2013**, *38*, L06605. doi:10.1029/2011GL046827.

12. Xiao, W.; Liu, Y.; Wu, G.; Yue, D. Rogue wave occurrence and dynamics by direct simulations of nonlinear wave-field evolution. *J. Fluid Mech.* **2013**, *720*, 3357–3392. doi:10.1017/jfm.2013.37.

13. Fedele, F.; *et al.* Real world ocean rogue waves explained without the modulational instability. *Sci. Rep.* **2016**, *6*, 27715. doi:10.1038/srep27715.

14. Fedele, F.; Lugni, C.; Chawla, A. The sinking of the El Faro: predicting real world rogue waves during Hurricane Joaquin. *Sci. Rep.* **2019**, *7*, 11188.

15. Brennan, J.; Dudley, J.; Dias, F. Extreme waves in crossing sea states. *International Journal of Ocean and Coastal Engineering* **2018**, *1*, 1850001. doi:10.1142/S252980701850001X.

16. Janssen, P. Nonlinear Four-Wave Interactions and Freak Waves. *Journal of Physical Oceanography* **2003**, *33*. doi:10.1175/1520-0485(2003)33<863:NFIAFW>2.0.CO;2.

17. Fedele, F. Rogue waves in oceanic turbulence. *Physica D: Nonlinear Phenomena* **2008**, *237*, 2127 – 2131. Euler Equations: 250 Years On, doi:https://doi.org/10.1016/j.physd.2008.01.022.

18. Fedele, F.; Tayfun, M.A. On nonlinear wave groups and crest statistics. *Journal of Fluid Mechanics* **2009**, *620*, 221–239. doi:10.1017/S0022112008004424.

19. Fedele, F.; Cherneva, Z.; Tayfun, M.; Guedes Soares, C. Nonlinear Schrödinger invariants wave statistics. *Physics of Fluids* **2010**, *22*. doi:10.1063/1.3325585.

20. Ducrozet, G.; Gouin, M. Influence of varying bathymetry in rogue wave occurrence within unidirectional and directional sea-states. *J. Ocean Eng. Mar. Energy* **2017**, *3*, 309–324. doi:10.1007/s40722-017-0086-6.

21. Fedele, F.; *et al*. Large nearshore storm waves off the Irish coast. *Sci. Rep.* **2019**, *9*, 15406. doi:10.1038/s41598-019-51706-8.

22. Slunyaev, A.V. Effects of coherent dynamics of stochastic deep-water waves. *Phys. Rev. E* **2020**, *101*, 062214. doi:10.1103/PhysRevE.101.062214.

23. Tayfun, M.; Alkhalidi, M. Distribution of sea-surface elevations in intermediate and shallow water depths. *Coastal Engineering* **2020**, *157*, 103651. doi:10.1016/j.coastaleng.2020.103651.

24. Dommermuth, D. The initialization of nonlinear waves using an adjustment scheme. *Wave Motion* **2000**, *32*, 307–317. doi:10.1016/S0165-2125(00)00047-0.

25. Brennan, J.D. On the emergence of extreme ocean waves. PhD thesis, School of Mathematics and Statistics, University College Dublin, 2017.

26. Tayfun, M.A. Statistics of nonlinear wave crests and groups. *Ocean Engineering* **2006**, *33*, 1589 – 1622.

27. Barthelemy, X.; Banner, M.L.; Peirson, W.L.; Fedele, F.; Allis, M.; Dias, F. On a unified breaking onset threshold for gravity waves in deep and intermediate depth water. *Journal of Fluid Mechanics* **2018**, *841*, 463–488. doi:10.1017/jfm.2018.93.

28. Derakhti, M.; Banner, M.L.; Kirby, J.T. Predicting the breaking strength of gravity water waves in deep and intermediate depth. *J. Fluid Mech.* **2018**, *848*.

29. Dommermuth, D.G.; Yue, D.K.P. A high-order spectral method for the study of nonlinear gravity waves. *Journal of Fluid Mechanics* **1987**, *184*, 267–288. doi:10.1017/S002211208700288X.

30. West, B.J.; Brueckner, K.A.; Janda, R.S.; Milder, D.M.; Milton, R.L. A new numerical method for surface hydrodynamics. *Journal of Geophysical Research: Oceans* **1987**, *92*, 11803–11824. doi:10.1029/JC092iC11p11803.

31. Tanaka, M. A method of studying nonlinear random field of surface gravity waves by direct numerical simulation. *Fluid Dynamics Research* **2001**, *28*, 41 – 60. doi:https://doi.org/10.1016/S0169-5983(00)00011-3.

32. Rapp, R.J.; Melville, W.K. Laboratory Measurements of Deep-Water Breaking Waves. *Philosophical Transactions of the Royal Society of London. Series A, Mathematical and Physical Sciences* **1990**, *331*, 735–800.

33. Tian, Z.; Perlin, M.G.; Choi, W. Energy dissipation in two-dimensional unsteady plunging breakers and an eddy viscosity model. *Journal of Fluid Mechanics* **2010**, *655*, 217–257.

34. Tian, Z.; Perlin, M.; Choi, W. An eddy viscosity model for two-dimensional breaking waves and its validation with laboratory experiments. *Physics of Fluids* **2012**, *24*, 036601–036601–23. doi:10.1063/1.3687508.

35. Tolman, H.; Group, D. *User manual and system documentation of WAVEWATCH III version 4.18*; 2014; p. 282.

36. Chawla, A.; Spindler, D.M.; Tolman, H.L. Validation of a thirty year wave hindcast using the Climate Forecast System Reanalysis winds. *Ocean Modelling* **2013**, *70*, 189–206. doi:10.1016/j.ocemod.2012.07.005.

37. Janssen, P.A.E.M. On some consequences of the canonical transformation in the hamiltonian theory of water waves. *Journal of Fluid Mechanics* **2009**, *637*, 1–44.